Advanced Energy Systems and Intelligent Geoscience (AESIG)
https://www.mospbs.com/journal/aesig

• *Article* •

A Numerical Study of Hydraulic Fracture Growth Under One Cyclic Injection

Seqiang Zhuo[1,2], Zaile Zhou[3,4,*], Yinglun Qin[1,2], Yuzhu Kang[1,5], Hui Zhao[3,4], Lie Kong[6], Zhihong Kang[7]

[1] Guangxi Shale Gas Benefit-Oriented Exploration and Development Academician Workstation, Nanning 53020, China.

[2] Guangxi Shale Gas Exploration and Development Co., Ltd, Liuzhou 545002, China.

[3] School of Petroleum Engineering, Yangtze University, Wuhan 434023, China.

[4] Hubei Key Laboratory of Drilling and Production Engineering for Oil and Gas, Yangtze University, Wuhan 430100, China.

[5] Petroleum Exploration and Production Research Institute, Sinopec, Beijing 102200, China

[6] Department of Mechanical, Aerospace and Civil Engineering, University of Manchester, Manchester, United Kingdom.

[7] Energy College, China University of Geosciences (Beijing), Beijing 100083, China.

[*]**Corresponding Author:** Zaile Zhou **Email:** zhouzaile@yangtzeu.edu.cn

Received: 10 February 2026 **Accepted:** 13 February 2026

Abstract: In this paper, a more potential cyclic fracturing scheme, which alternates injection and flowback in each injection cycle, is proposed to promote the stimulation efficiency. Collection and Re-injection of all the flowback fluid into formation to create fractures in the following cycles achieves environmental sustainability. With 2D displacement discontinue method, we model the dynamic behavior of a bi-wing fluid-driven fracture symmetrically emanated from a circular wellbore under the proposed cyclic injection schedule. The results show the fracture continues to propagate despite a flowback operation. A depressurization operation by fast flowback renders the closure of the fracture mouth and pushes up the pressure of the fluid sealed inside the fracture; When restarting the injection, a pressure trough exists along the fracture path and moves towards the fracture tip until the fracture growth resumes. Under the operation of cyclic injection, even deep inside the fracture, it generates cyclic pressure amplitude comparable to the amplitude of injection pressure. The parametric study reveals that a smaller stress difference impairs the fracture mouth width; Low fracture toughness stunts the impact of a cyclic injection rate change on the fracture growth. The relation between the injection pressure and the cumulative fluid volume appears independent of cyclic injection schedules if the product of injection rate and fluid viscosity in each counterpart phase is the same. With fracture growth and no successive cyclic injection,

DOI: https://doi.org/10.58244/aesig.263587

the injection pressure tends to follow the curve generated from constant-rate injection cases.
Keywords: Cyclic injection; Flowback; Behavior of fracture; pressure amplitude; Fracture re-opening; Injection schedule

List of Symbols

σ_1,σ_2	Maximum and minimum far-field stresses	μ	Fluid dynamic viscosity
r	Wellbore radius	t	Injection time
l_f	Length of fracture branch	p	Internal fluid pressure of fracture
L_f	The distance from the tip of the fracture to the center of the wellbore	G_{11},G_{12}, G_{21}, G_{22}	Hypersingular Green's functions
P_w	Wellbore pressure (injection pressure)	q_o	Total wellbore injection rate
E	Young's modulus	q_i	The influx of each fracture branch
ν	Poisson's ratio	U	Volumetric compliance of the injection system
K_{IC}	Fracture toughness	K_m	Dimensionless fracture toughness
N	Fracture branch number	Q_i	The ith injection rate value
w,v	Fracture opening and shear displacements across fracture surfaces	T_i	Starting time array of the ith injection rate value
σ_n,τ	Normal stress and shear stress on the fracture surface	P_{fi}	Pressure at the ith fracture branch mouth
σ_{fn},τ_{fs}	Resultant normal and shear components generated by the far-field stresses	l_{fi}	Length of the ith branch fracture

1 Introduction

Hydraulic fracturing, which creates fractures in deep formations by the highly-pressurized fluid, has become a necessary technique to extract many geo-energies and geo-resources such as unconventional oil and gas, geothermal energy, and deep dissolvable minerals (via in-situ leaching) [1-3]. As fracture is a high permeable flow path, a longer or geometrically more complex fracture/fracture network is beneficial to the mining productivity. It has been consented that the injection scheme is an important factor that affects the fracture geometry. Traditionally, an injection scheme with a constant injection rate is mostly used [4]. However, this injection scenario could only result in limited fracture length/complexity and it has a possibility to induce high-magnitude seismic events in the formation [5]. Comparatively, cyclic injection fracturing (CIF), which adopts a cyclically changing injecting rate, could create elevated hydraulic fracture length/complexity and some studies have found its potential in minimizing the induced seismicity [6, 7].

The invention of cyclic fracturing dates back to 1959 when Hulse found that a fracturing process with superimposed cyclic pressure could be used to improve the stimulation efficiency for oil & gas reservoirs [8]. After a few decades of research and development, cyclic fracturing has developed into a family with varying injection

scenarios. Specifically, it can be implemented in two categories: injection-rate control and injection-pressure control. Amongst, each kind of cyclic injection can be subdivided into multiple variant types. Depending on whether the peak injection rate or pressure in each cycle is constant or not, the CIF can be classified as constant-injection rate or -pressure type or stepwise-rate or -pressure type [9]. Depending on whether the cyclic frequency is constant or not, the CIF can be classified as an equal-frequency type or variable-frequency type [7]. Moreover, if a pulse pump is connected to the injection system, then it can be extended to pulse fatigue fracturing in a broader sense, with a wide application for the stimulation of coal seam [10-12]. For the injection-pressure controlled type, so-called pre-breakdown cyclic injection, its priority aim is to reduce the breakdown pressure for reservoirs whose rock has very high strength (e.g. granite). Often there is no fracture initiated amid the cyclic injection before the total breakdown of the wellbore, thus it is suitable for hot-dry rock in geothermal development [2]. In the CIF controlled by the injection rate (so-called post-breakdown cyclic injection), the fractures can be initiated in the first cycle, but creating complex fracture networks is taken as the prior purpose.

The stepwise-rate CIF could significantly reduce the magnitude of the induced seismic events in the enhanced geothermal systems [13-18]. It is found that the CIF with constant upper-bound pressure could reduce the initiation pressure by 40% [6]. Among different types of CIFs for the stimulation of EGS, the stepwise pulse pressurization-controlled type achieves higher injectivity; cyclic progressive injection gets the best effects to relieve induced seismicity but with relatively low injectivity. While cyclic pulse pressurization retains the relative balance of the injectivity and seismic risk [9]. Similar CIF tests for the sandstone materials show that more acoustic emission (AE) events and more obvious micro-damage with higher permeability, were generated compared with the conventional continuous injection [19]. The constant-rate CIF tests with concrete blocks as specimens demonstrates that cyclic injection can help to generate multiple fractures; moreover, the variable-frequency CIF can further promote the complexity of the fractures compared with the constant-frequency scenario [7]. Then through similar CIF experiments for the concrete specimens with multi-cluster perforations, it reveals that the cyclic injection could initiate more perforation clusters and create several main hydraulic fractures in one treatment. In those experiments, the subsequent injection cycle produced a higher peak pressure than the breakdown pressure in the first cycle. This abnormality has also been reported in the oil field [15, 20].

The above research on cyclic injection mainly focuses on reducing the breakdown pressure and relieving seismic events during a fracturing operation. It is known that a higher amplitude of the cyclic load can significantly accelerate fatigue failure of rock material [21-23]. Similarly, enhancing the amplitude pressure of the CIF can promote the creation of multiple fractures in as few cycles as possible, although the mechanism is much more complex than rock fatigue theory. However, the injection-pressure controlled CIF has a very limited adjustment for pressure amplitude, and oblivious difficulty to accommodate the existing fracturing equipment on-site. Instead, we focus on the injection-rate controlled CIF, with higher field compatibility. Often the peak injection pressure is principally determined by the geological conditions of the reservoir. While the valley pressure can be reached depends on the fluid filtration rate into formation against the valley injection rate. Without any intervention, even for zeros

injection rate, the valley pressure usually slowly declines to near the minimum principal stress with time elapses [24-27]. To further increase the pressure amplitude, an aggressive cyclic injection and alternating flow-back (CIAF) method can be tried by performing flowback immediately after suspending the injection in each cycle, which provides an impetus to reduce the injection pressure rapidly to the lowest value (i.e. the hydrostatic pressure in theory).

Particularly, the fracture behavior subject to cyclic injection is an extremely complicated process. This issue involves many sub-processes such as the redistribution of the fluid pressure in fracture, real-time changing of fracture opening, and the re-allocation of the injection flux among multiple fractures. Many underlying mechanisms associated with fracture behaviors are still not fully explored. In this article, we take CIAF for research to model the hydraulic fracture patterns under cyclic injection schedules and perform a parametric study about the cyclic fluid injection and fracture growth. The overall growth characteristics of the symmetric fractures are considered instead of the prohibitively complex multiple fractures growth under cyclic injection.

2 Numerical methodology

The physical process during CIAF fracturing is complex. It is a fully coupled hydro-mechanical problem where fluid flow and deformation of solid rock are highly dynamic. Specifically, one cycle of CIAF may involve fracture initiation and propagation. This is followed by an immediate suspension of fluid injection and then fluid flowback. In some situations, the created hydraulic fracture may re-close dynamically after suspension of fluid injection. After restarting the injection, the existing fracture will reopen and propagate.

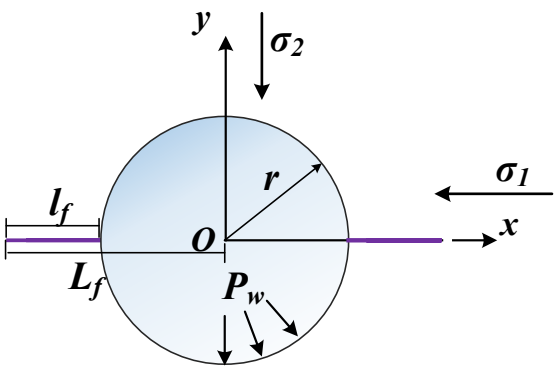

Fig.1 Configuration of a fracture emanating from an open-hole wellbore

To simulate this problem, we adopt the 2D displacement discontinuity method (DDM) [28] in this study. We present the assumption, formulation, and model verifications that are used to simulate the dynamic behavior of hydraulic fractures in the CIAF fracturing.

2.1 Governing Equations

A bi-wing fracture geometry from a wellbore is considered to simulate the CIAF fracturing. Fig.1 shows the model configuration and the Cartesian coordinate system. The reservoir is considered an infinite elastic medium. Two wings of the fracture are assumed to be along the x-axis with their length denoted as l_f. A wellbore is in the center whose radius is r. The distance between the wellbore center and the fracture tip is denoted as L_f. The injection pressure inside the wellbore is denoted as P_w. Plane-strain deformation is assumed in the simulation. The two far-field stresses [σ_1 and σ_2 ($\sigma_1 \geq \sigma_2$)] are set to along the x and y directions, respectively.

The main assumptions are summarized as follows:

The rock matrix is isotopic and impermeable;

The fracture surface is smooth, and no fluid lag is allowed in the process;

Fracturing fluid is an incompressible Newtonian fluid;

The elastic integral equations for the stress balance on the wellbore and the fracture surface can be expressed as [29-31]:

$$\begin{cases} \sigma_n(x,y)-\sigma_{fn}(x,y)=\left(\sum_{i=1}^{N}\int_0^{l_{fi}}+\oint_C\right)G_{11}(x,y,s)w(s)+G_{12}(x,y,s)v(s)ds \\ \tau(x,y)-\tau_{fs}(x,y)=\left(\sum_{i=1}^{N}\int_0^{l_{fi}}+\oint_C\right)G_{21}(x,y,s)w(s)+G_{22}(x,y,s)v(s)ds \end{cases} \quad (1)$$

where N (=2) is the number of fracture wings and C is the circumference of the wellbore. w and v are the fracture opening and shear relative displacement across two faces of the fracture, respectively. s is the point location along the fracture path. σ_n is the normal stress which usually equals the fluid pressure; τ is the shear stress on the fracture surface and it vanishes locally when the surfaces are separated from each other. σfn and τ_{fs} are resultant normal and shear components generated by the far-field stresses. l_{fi} is the length of each fracture with the subscript i denoting the branch number. G_{11}, G_{12}, G_{21}, and G_{22} are the corresponding hypersingular Green's functions.

It must be noted that fracture closure is possible during flowback. The flow of fluid in fractures can be divided into two forms. One is fluid flow through an open channel. The other form is along with closed fracture segments. This form can be considered a weak coupling between the solid deformation and fluid. The equations for describing flow in close fracture portions can be found in the previous work[32], which is written as

$$\frac{\partial p_f}{\partial t}-c\frac{\partial}{\partial s}\left(\omega^2\frac{\partial p_f}{\partial s}\right)=0 \quad (2)$$

Where, ω is the fracture initial aperture (or fracture closure aperture) and c is the pressure conductivity factor of the close fracture. Reynolds' lubrication equation is used to describe fluid flow in an open fracture channel, expressed as

$$\frac{\partial w}{\partial t}=\frac{\partial}{\partial s}\left(\frac{w^3}{12\mu}\frac{\partial p_f}{\partial s}\right) \quad (3)$$

where t is the injection time; p is the fluid pressure in fracture; μ is the fluid dynamic viscosity. The fluid flow is controlled by the injection rate q_o, which contributes to the fracture volume and wellbore storage. According to Eqs. (1), (2) and (3), the normal and the shear displacements at a place can be coupled to the fluid flow rate through the computation of local fluid pressure in fracture.

2.2 Fracture Growth

According to the displacement correlation method [33], the stress intensity factors (SIFs) of modes I and II fracture growth can be expressed as:

$$\begin{cases} K_I=\dfrac{\alpha E\sqrt{\pi}}{4(1-\nu)\sqrt{2r_{tip}}}w(r_{tip}) \\ K_{II}=\dfrac{\alpha E\sqrt{\pi}}{4(1-\nu)\sqrt{2r_{tip}}}v(r_{tip}) \end{cases} \quad (4)$$

where rtip is the half-length of the element at fracture tip; E is Young's modulus; ν is Poisson's ratio. Since the singular element is used at the fracture tip in the computation, the coefficient α is approximately equal to 0.806[34]. For the mixed-mode fracture growth, the deflection direction of the fracture can be determined by[35]:

$$K_I\sin\Theta+K_{II}(3\cos\Theta-1)=0 \quad (5)$$

where Θ represents the deflection angle from the current fracture line. When the fracture extends in a mixed mode, the stress intensity factor must meet the following condition [35]:

$$\cos\frac{\Theta}{2}\left(K_I\cos^2\frac{\Theta}{2}-\frac{3}{2}K_{II}\sin\Theta\right)=K_{IC} \quad (6)$$

where K_{IC} is fracture toughness.

2.3 Initial boundary conditions

For hydraulic fracture growth from the wellbore, an initial notch is given to the fracture wings at the beginning to lead the fracture to grow along the x-axis direction. Initially, two notches are assumed to be empty of fluid, and the rock matrix is assumed to be in static equilibrium under the applied principal stresses σ_1 and σ_2. The sum of influxes from the borehole should satisfy:

$$\sum_{i=1}^{N} q_i(0,t) = q_0 - U\frac{\partial P_w}{\partial t} \tag{7}$$

where, q_i is the influx of each fracture wing, m^2/s; q_o is the total injection rate at the wellbore, m^2/s; U is volumetric compliance of the injection system., U can be identified by the initial linear slope of the injection pressure vs injection fluid volume curve at low pressure, m^2/MPa [36, 37].

2.4 Numerical algorithm

For the elastic equations, the displacement discontinuity method (DDM) [28] is used and both the wellbore and fractures are discretized into constant-length DD elements. Based on the same mesh, the Reynolds' lubrication equation is solved by the finite volume method (FVM).

The implicit method is used to solve for the displacements across fracture surfaces by incorporating the elasticity equations into Reynold's lubrication equation to obtain an integral-differential equation. In addition, the backward Euler method is used for the time discretization and an explicit time step is used in the computation.

The numerical method used a fixed element length for regular elements. To improve the accuracy of SIFs, the three elements immediate at the fracture tips take the half size of the regular elements. This adaptive mesh scheme is implemented in fracture growth [32]. Moreover, to eliminate the rigid-body motion of the pseudo-material caused by the adoption of DDM, two elements with different orientations are added inside the wellbore and their movements are fixed throughout the computation [38].

When the propagation criterion is satisfied, the fracture tip is extended by an increment with the size of a regular element. The direction of the new increment is determined by Eq. (5). The combination of a fixed fracture increment with a small-time step can be adjusted based on the advancement of the fluid front, which is found capable of ensuring solution convergence for the coupled equations.

2.5 Model Verification

To verify the proposed numerical model, we selected the results by Lecampion et al [39] as reference. They considered similarly a bi-wing fracture emanating from a wellbore model under the same boundary conditions as ours. In their work, they have used a fine mesh and we considered two situations with 120 elements and 180 elements, respectively. Fig.2 shows the fracture width distributions over the fracture length in the referring results and with our two settings of element number. The red dashed curve

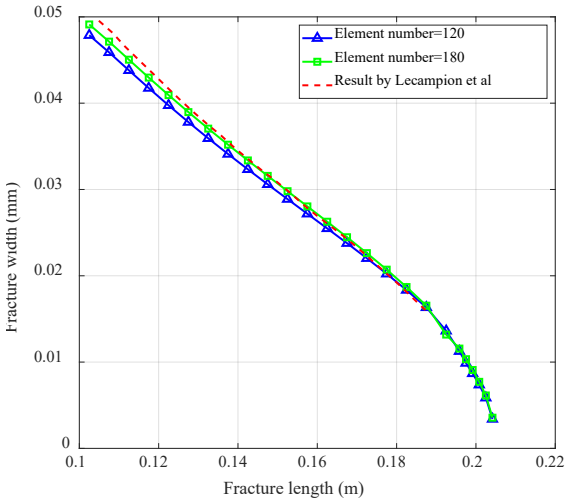

Fig.2 Fracture width comparison of a bi-wing fracture emanating from a wellbore

denotes the numerical results of fracture width from the 1DPlanarHF code by Lecampion et al [39]. Generally, a higher calculation accuracy can be obtained by using more elements. However, a higher number of elements will result in increasing computation loads. A balance between the number of elements and the computation should be a stroke in simulation practices. Compared with the results using 120 elements, using 180 elements can provide higher accuracy when calculating the hydraulic fracture width. In addition, it can be seen that 180 elements could provide sufficient accuracy referring to the results obtained by Lecampion et al [39] which used a very fine mesh. In the following sections, 180 elements are used to discretize the wellbore with a fixed radius of 0.1 m.

3 General fracturing behaviors by CIAF

In our proposed CIAF method, each injection cycle was accompanied by firstly injecting and then a pause. The pause of injection allows the hydro pressure to release. In the simulation, we simplify the process of injection pause. Specifically, the pressure relief operation is assumed to be complete immediately after suspending the injection. The flow rate during the pressure relief is taken as a negative constant value. The simplification can be reasonable and does not affect the overall behavior trend of fracture in flowback.

During CIAF, several sub-processes are expected which include (1) the closure of the fracture after suspending the injection and fluid flowback, (2) a pause of zero injection rate, and (3) reopening and growth of the existing fracture after restarting fluid injection. To simulate the CIAF, it is imperative to capture these sub-processes in one model.

The model setup and basic parameters used in the presented study are listed as follows: the radius of the wellbore r=0.1 m, the initial notch length l_f=0.09 m, the elastic modulus of the reservoir E=19.0 GPa, the Poisson's ratio ν=0.14, the fracture toughness K_{IC}=1.0 MPa•$m^{0.5}$, the fluid viscosity μ=0.01 Pa•s, the initial notch aperture ω=1.0×10^{-6} m which always exist even when the fracture surfaces get closed. The volumetric compliance of the injection system U is fixed as 1.2×10^{-6} m^2/MPa. The values of the far-field stresses σ_1 and σ_2 are 2.8 MPa and 2.0 MPa, respectively, if no otherwise is specified. Note that comparatively low far-field stresses are used here. However, this will not affect the results, because it is the net pressure that dominates the dynamic characteristics of the fractures [40]. The injection schedule marked as S1 of an injection & flowback cycle is shown in Table 1, where T_{i-1} and Ti are the starting time and the end time of the total injection rate Q_i. For convenience, the flow rate Q_i is stipulated as positive for the normal injection segment and denoted as negative for the flowback segment. In each injection schedule, the flow rate Q_1 is adopted for the initial injection phase in the time interval $T_0 < t < T_1$; as well as the injection rates denoted as Q_2, Q_3, Q_4 are used for the depressurization phase of $T_1 < t < T_2$, zeros injection-rate phase of $T_2 < t < T_3$, re-injection phase of $t > T_3$,

Table 1 The CIAF injection schedule S1

Time t (s)	$T_0 \le t < T_1$	$T_1 \le t < T_2$	$T_2 \le t < T_3$	$t \ge T_3$
	0 ~ 0.253	0.253 ~ 0.390	0.390 ~ 0.427	≥ 0.427
Flow rate q (m^2/s)	Q_1	Q_2	Q_3	Q_4
	2.0×10^{-4}	-3.2×10^{-4}	0	2.0×10^{-4}

respectively. To guarantee the numerical iterative convergence, an intermediate flow rate with a very short transient period of not more than 0.005s is inserted as a transition to smooth the sharp flow change.

Among those cases using this injection schedule S1, the case CN0 is used as a base case for comparisons, and the injection schedule S1 is also used for the cases CS1~CS5 with different principal stresses and CK1~CK5 with the cases but with different material parameters.

What needs to be clear is that a large injection rate is often used to match a larger time scale. In our model, as the relatively small fracture length is used, a small-time scale is chosen to reproduce the fracturing behaviors in simulation. If it is needed, the time scale can be enlarged to the real injection time scale[41]. For the mechanism study, the time scale is not very important for the case study. To better capture the dynamic behavior of the fracture, the injection schedule is deliberately chosen, for example, the fracture mouth width cannot be exactly equal to zero, and wellbore pressure cannot be too low after flowback. However, the injection schedule can be modified to consider more complex cases.

The numerical results of case CN0 under the injection schedule S1 with different injection phases distinguished by colored shadows are displayed in Fig.3. They include the developments of the injection pressure and fracture mouth width over time. Initially, the injection pressure rises almost linearly before the extension of the pre-set notch (Q_1: $T_0< t <T_1$ marked by blue shadow). After the injection pressure reaches the highest pressure, the

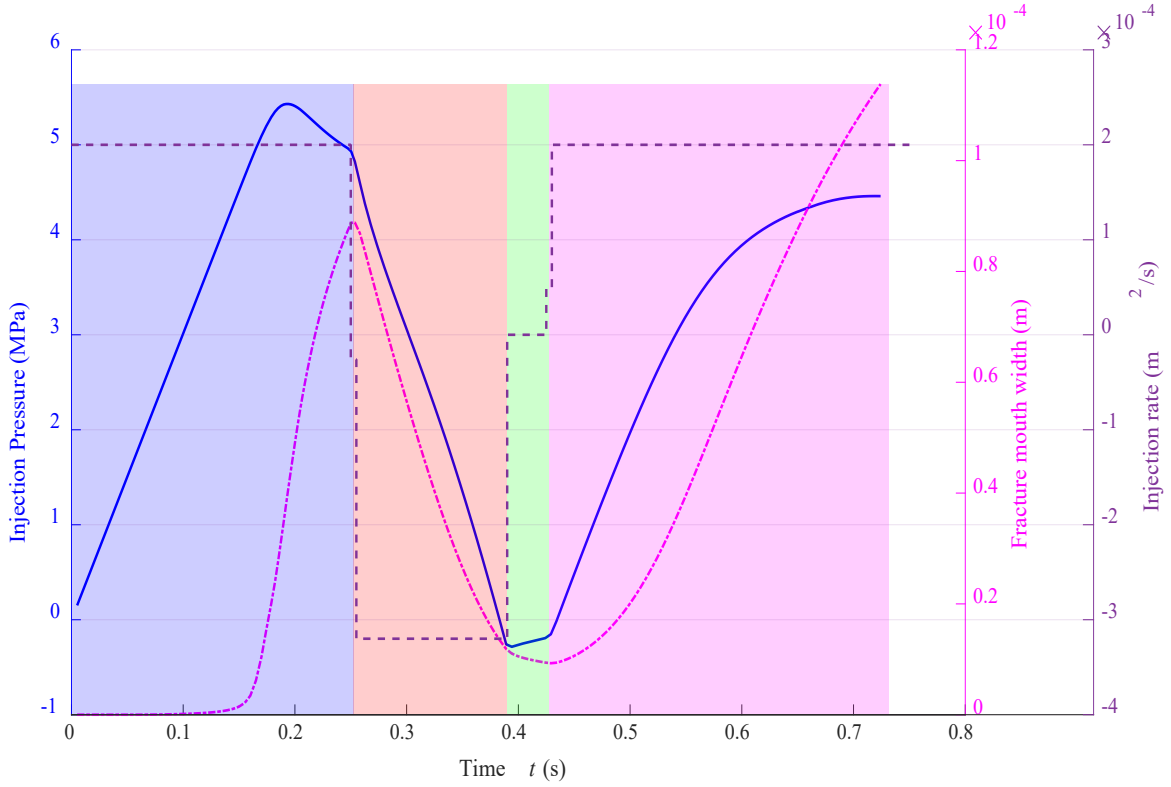

Fig. 3 The curve of the injection pressure and fracture mouth width vs time for the case CN0

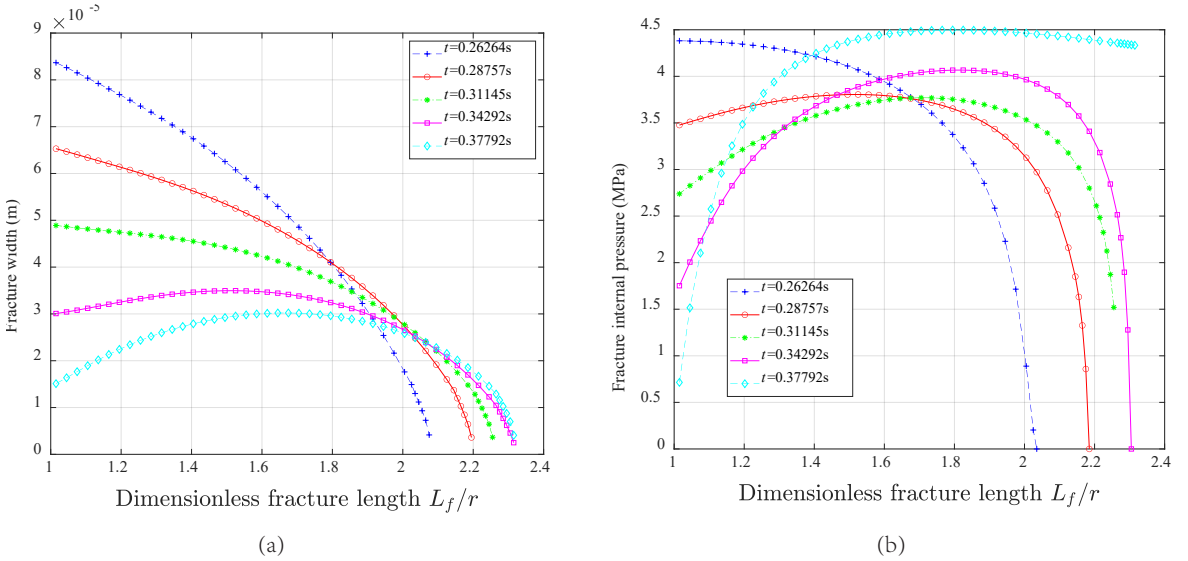

Fig.4 Evolutions of (a) pressure distribution within the fracture and (b) the fracture width along dimensionless fracture length (L_f / r) during the depressurization phase (T_1<t<T_2) (where L_f=l_f+r)

pressure starts to decline at a comparatively slow rate. While fluid flowback starts (Q_2: T_1< t <T_2 marked by orange shadow), the decreasing rate of the injection pressure becomes much higher. Once the fracture is initiated, the changing trends of the fracture mouth width, which are denoted by the opening of the fracture element closest to the wellbore, are always the same as that of the injection pressure. Note that there is a small negative value of injection pressure, which may require another constraint beyond the mass conservation given by Eq. (6). However, it does not affect the trend of numerical results. When the injection pressure quickly drops to around zero, a very small fracture mouth width is retained, which can severely retard out-flow of fluid flowing from fracture to the wellbore. After restarting the injection again (t > T_3), the injection pressure starts to rise. Accordingly, the width of the fracture mouth increases while the fluid pressure is recovering.

To further uncover the deformation of the fracture when out-flow is taking place (i.e. the depressurization phase of T_1< t <T_2), we plotted out the width and internal pressure along the fracture. The results are seen in Fig.4. It is found that although the injection pressure of the borehole was released during this stage, the length of the fracture does not decrease but keeps increasing (Fig.4(a)). This behavior can be very interesting as one of the principles of hydraulic fracturing in reservoir stimulation is to create a maximum fracture length. A more details discussion on this behavior is provided in the following context. During this stage(T_1< t <T_2), the fracture width substantially went down at the wellbore side, but slightly went up at the fracture tip. At the end of this phase, the fracture width profile has its peak at the middle of the fracture, indicating that some fluid gets stored in the fracture at the depressurization stage. Although the storage volume decreases over time, its rate of change appears to decrease too. In addition, the width of the fracture mouth seems to decrease at a larger rate. This means that for a long time the depressurization phase lasts, and the fluid captured inside the fracture cannot be fully squeezed out by the applied confining stress.

The internal pressure inside the fracture changes almost reversely compared to the fracture

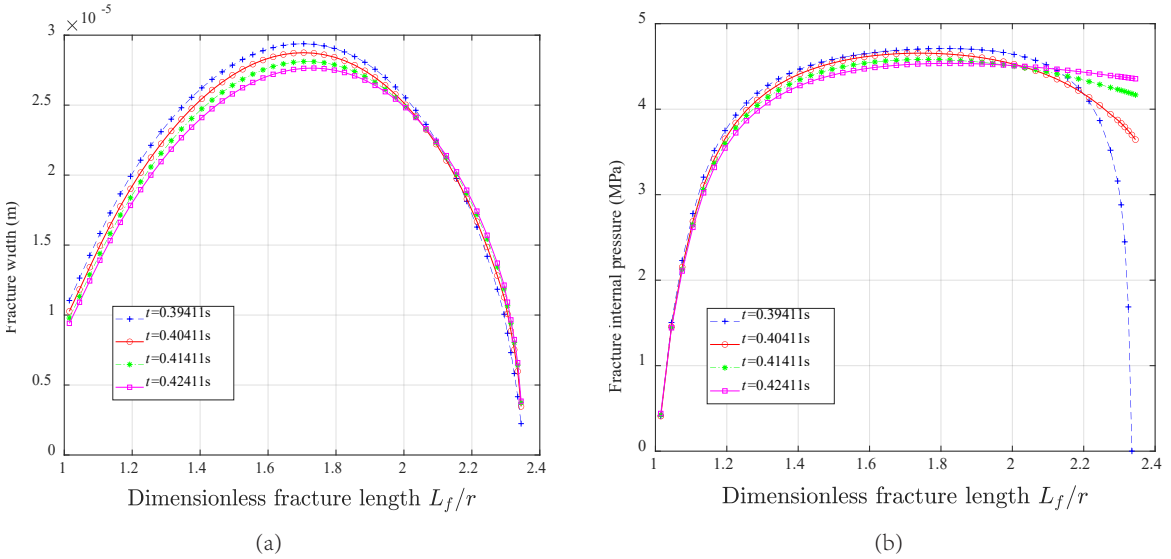

Fig. 5 (a) Fracture internal pressure distribution and (b) the fracture width distribution vs dimensionless fracture length (L_f / r) in zero injection-rate phase (T_2<t<T_3) (where L_f=l_f+r)

opening stage, as shown in Fig.4 (b). With the fracture volume decreasing, the resistance to the confining stress is offered by the fluid remaining in the fracture. This interaction results in some increases in the pressure inside the fracture. During the depressurization phase, the location of maximum pressure transfers from the fracture mouth to deep inside the fracture, as shown in Fig.4(b). In this depressurization phase by the flowback operation, the location deep inside the fracture path obtains its highest-pressure value, even much higher than the pressure in the initial injection phase. This means that a flowback operation would not deplete the internal pressure along the fracture path. Instead, a rapid flowback pushes up the pressure to a certain value, which can even be equivalent to the highest injection pressure at the wellbore. If there are nature fractures or weak layers along the fracture path, new fractures get a higher possibility to be initiated. Note that natural fracture and weak layers widely exist in many deep reservoirs such as shale, coal, and even EGS reservoirs[42-44].

During the zero injection-rate phase (i.e. Q_3: $T_2 < t < T_3$ marked by green shadow), the reverse flow from the fracture toward the well is constrained as a result of the closure of the fracture mouth. It implies that the fracture volume does not change significantly, nor does the fracture width, (see Fig.5(a)). Therefore, the internal pressure of the fracture is decreased within a limited range, as shown in Fig.5(b). It is worth noting that although the pressure at the fracture mouth is around 0.4 MPa, larger than the wellbore pressure (i.e. 0MPa), the fluid inside the fracture can still be sealed by the narrow width of the fracture mouth.

In the re-injection phase (i.e. Q_4: $t > T_3$ marked by magenta shadow), the pressure in the wellbore rises linearly at almost the same slope as that in the initial injection phase. With more fluid entering the fracture, the fracture width increases and restores a normal shape, as shown in Fig.6(a). The pressure distribution is plotted in Fig.6(b). As can be seen, after re-injection, as the wellbore pressure increase, there is an area with small internal pressure, which results in a concavely distributed pressure along the fracture. Specifically, at t= 0.58413s, the injection pressure

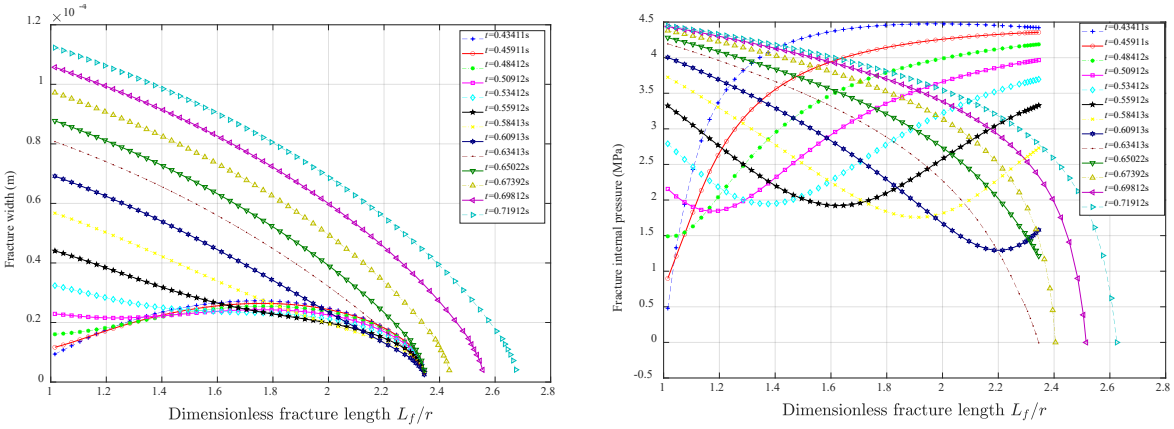

(a) (b)

Fig.6 (a) Fracture internal pressure distribution and (b) distribution of the HF width vs dimensionless fracture length (L_f/r) in re-injection phase($t>T_5$)

at the borehole becomes the maximum along the length dimension. This concave area of internal pressure was initially located near the borehole, and it keeps moving forwards to the fracture tip over time. After then, pressure distribution along fracture becomes a mono-decreasing function over length. The width of fracture around the near-borehole area remains increasing. After the low-pressure area propagates to reach the fracture tip, the re-growth of fracture length gets recovered. It can be expected that the above-described fracturing dynamics may be repeated during the multiple injection cycles. Therefore, we only consider two injection cycles here to reveal the principal behaviors.

For CIAF, the hydraulic fracture is subject to repeatedly pressurizing and depressurizing. To identify the range of pressure change within the fracture, we plotted the upper and lower bounds for fluid pressure along the fracture path in Fig.7. It should be mentioned that the fluctuations in the hydraulic pressure by multiple cyclic loads may cause damage of defects in formations given mechanical heterogeneities exist.

We deliberately avoid taking the internal pressure of a rapidly expanding fracture as the bound value since this type of internal pressure often occurs only once in the fracture creation stage rather than appearing frequently in the afterward cycles. We plot the change of the internal fracture pressure within one cycle along the fracture length. The upper and lower bounds of the pressure change inside the fracture are represented by the blue solid line and the red dotted line, respectively, as shown in Fig.7. Notably, the upper bound of the hydraulic fracture change is a multi-segment broken curve rather than a smooth curve, and the highest pressure endured along

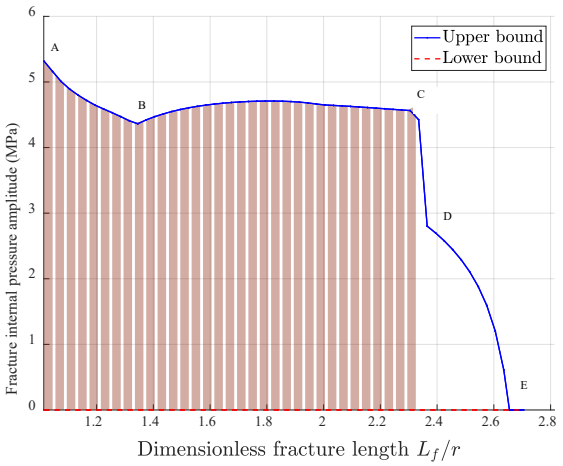

Fig.7 Amplitude of the dynamic fluctuation of internal pressure along the fracture path of CIAF

the fracture path represented by each broken line segment is induced by different injection stages. In the upper bound line, the pressure in the A-B segment of the fracture is created when the wellbore pressure reaches its peak in the re-injection phase. The B-C fracture section is brought about by the squeezing of the fluid sealed inside the fracture in the depressurization or zero injection-rate phases. While the low boundary of pressure can be close to the hydrostatic pressure of the wellbore (e.g. zero pressure in our model). As shown in Fig.7, we use the orange bars to represent the repeatable range of pressure changes along the fracture path. Since the C-D-E segment is a new growth fracture part in this cycle, and the pressure only appears only one time at the fracture-extending moment rather than in every cycle, the section C-D-E near the fracture tip is out of our focus.

Moreover, the internal pressure leveling off in the middle B-C segment of the fracture, displays a small difference with the pressure amplitude of point A at the fracture mouth. Notably, it implies that even deep inside the fracture, the pressure loading on the fracture surface is in a cyclic variation state with a comparable amplitude in contrast with the injection pressure amplitude. For the field fracturing operation through the CIAF, the variation range of the internal fluid pressure fluctuates between the minimum principal stress and the peak injection pressure. Often a higher net pressure is accompanied by a larger amplitude of the cyclic pressure. The pressure fluctuation can facilitate subcritical fracture growth from the rock matrix flaws [45-48]. Especially when there are sizable defects around the borehole or main fracture wall, the subcritical fracture growth can significantly reduce the threshold to create new fractures.

4 Parametric Studies

The above section has uncovered the general fracturing behaviors under the CIAF. In application, there can be a range of influential parameters that may lead to varying fracturing dynamics. We conduct parameter studies based on the developed CIAF numerical scheme. Specifically, the influence of the factors including the in-situ stresses, fracture toughness, and injection parameters are analyzed.

4.1 In-situ stresses

In-situ stress has a prominent influence on the injection pressure and subsequent propagation of fracture [49]. In this series of simulations, five pairs of stress combinations with variable stress differences $\Delta\sigma$ are used as listed in Table 2. In this part, the injection schedule S1 and the other parameters are the same as those in case CN0.

From Fig.8(a), one sees that the fracture opening becomes slightly wider with increasing $\Delta\sigma$. The increase of the in-situ stress σ_1 parallel to the

Table 2 Varying in-situ stresses used to analyze its role in CIAF fracturing

No.	σ_1 (MPa)	σ_2 (MPa)	$\Delta\sigma$ (MPa)	$\sigma_{\theta\theta min}$ (MPa)
CS1	2.8	2.0	0.8	3.2
CS2	3.8	2.0	1.8	2.2
CS3	4.8	2.0	2.8	1.2
CS4	5.8	2.0	3.8	0.2
CS5	6.8	2.0	4.8	-0.8

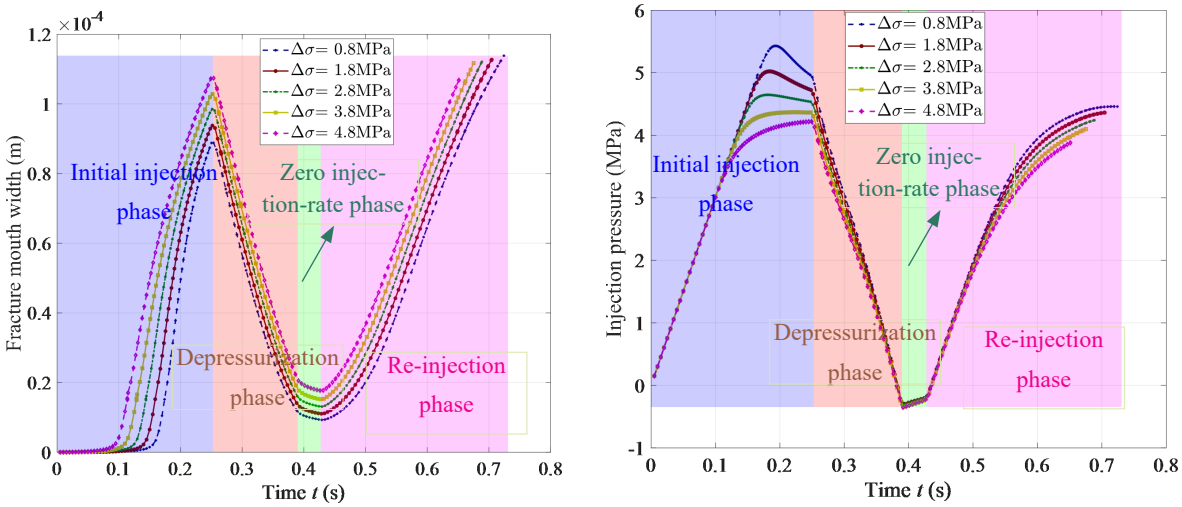

(a) (b)

Fig.8 (a) Fracture mouth width vs time and (b) injection pressure vs time under different stress combinations for cases CS1~CS5

fracture can reduce the confining stress across the fracture near the borehole. In Fig.8(b), it is shown that the peak injection pressure reduces with increasing σ_1. A higher value of $\Delta\sigma$ also facilitates fracture growth despite the same minimum stress across the fracture surface. It is further noted that, except for the maximum pressure in the initial cycle of injection, the injection pressure disparity is also much less than the stress difference $\Delta\sigma$ for the five pairs of in situ stresses used. In particular, the length of hydraulic fractures still continues to increase during fluid flowback regardless of different stress conditions, as shown in Fig.9. The fracture initiation occurs earlier with increasing σ_1. Although fracture keeps propagating at the early depressurization phase, the fracture length is frozen later in the zero injection-rate phase, and it maintains for quite a while even after the beginning of the re-injection phase. It is also noted that the restarting time of fracture growth seems not sensitive to the in-situ stress.

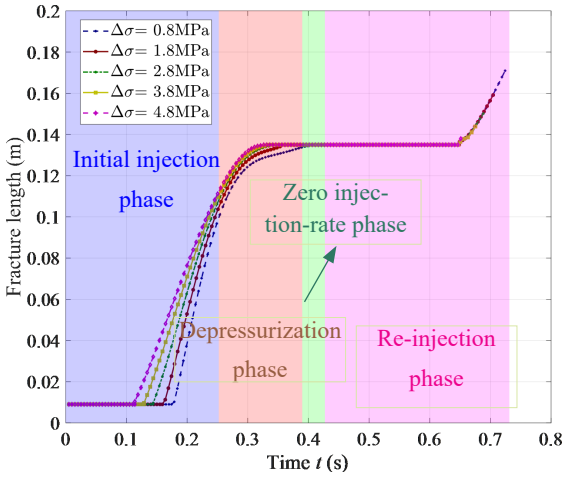

Fig.9 Fracture length vs time under different stress combinations for cases CS1~CS5

4.2 Fracture toughness

To consider the contributions of the material parameters, the dimensionless fracture toughness K_m is used. It is expressed as[40]:

$$\kappa_m = K'\left(\frac{1}{E'^3\mu' q_o}\right)^{1/4} \tag{7}$$

where the material parameters μ′、E′、K′ are defined as:

$$\mu' = 12\mu,\ E' = \frac{E}{1-\nu^2},\ K' = 4\left(\frac{2}{\pi}\right)^{1/2} K_{IC}$$

Here, the dimensionless fracture toughness

Table 3 Different fracture toughness used to analyze its role in CIAF fracturing

No.	K_{IC} (MPa•m$^{0.5}$)	K_m
CK1	0.2	0.148
CK2	0.4	0.295
CK3	0.6	0.443
CK4	0.8	0.591
CK5	1.0	0.738
CK6	1.2	0.886

K_m is calculated assuming that q_o equals the initial flow rate value Q_1 in the CIAF schedule.

We still use the injection sequence S1 and the same other parameters of the base case to study the effect of the fracture toughness on fracturing patterns, as the numerical cases listed in Table 3.

Fig.10 shows the effect of fracture toughness over the developments of fracture mouth width and injection pressure. It can be seen from Fig.10(a) that the fracture mouth width is almost the same and insensitive to the fracture toughness despite a totally different fracture growing pace. This may indicate that the fracture mouth width is irrelevant to the fracture length. Although the fracture toughness magnitude covers a wide range, the injection pressure also demonstrates only a slight change as shown in Fig.10(b).

It is anticipated that smaller fracture toughness is an impetus for a faster fracture propagating speed. Therefore, from Fig.11, the fracture length would be larger all the time under a smaller fracture toughness, given a fracture has been initiated (i.e. after t=1.73424 s). When the fracture toughness is low enough ($K_{IC} \leq 0.4$ MPa•m$^{0.5}$), the hydraulic fracture still extends forwards even in the depressurization phase and zero-injection phase, as shown in Fig.11. It demonstrates that fracture growth within a lower fracture-toughness matrix is more difficult to be stunted by the varying injection rate.

Specifically, the fracture propagation feature can be divided into four regions using black dotted lines A, B and C, as shown in Fig.11. Amongst, the fracture is in a relatively high-speed growth state at the moment before line A. Moreover, when $K_{IC} \geq 0.8$ MPa•m$^{0.5}$, in the incipient stage of the flowback, the fracture can still grow at a

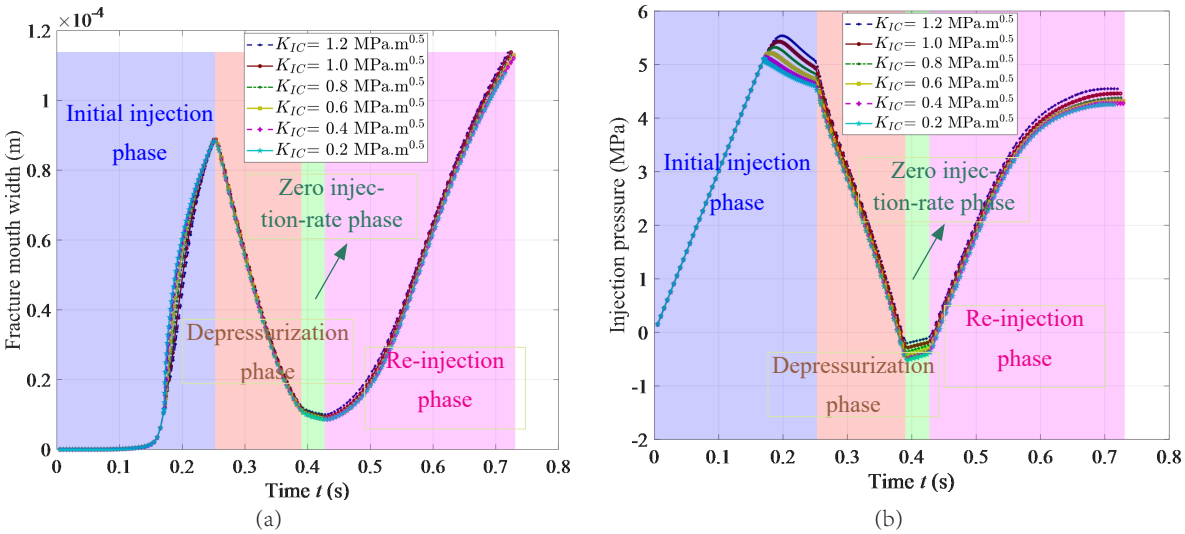

(a) (b)

Fig.10 (a) Fracture mouth width vs time and (b) injection pressure vs time under different fracture toughness (cases CK1~CK6)

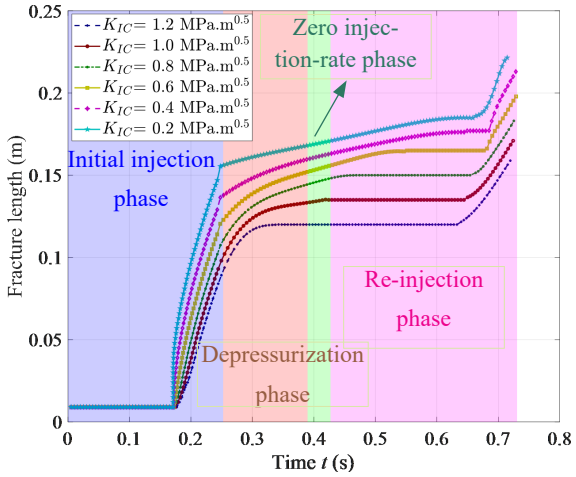

Fig.11 Fracture length vs time with the increasing fracture toughness for cases CK1~CK6

high speed. The region spans the initial injection phase and the depressurization phase. If the moment is between the dashed lines A and B, the fracture growth rate begins to slow down due to the flowback function transmitted to the fracture tip. When K_{IC}<0.8 MPa•m$^{0.5}$, slow-speed growth of the fracture crosses three spans including the depressurization phase, the zero-injection rate phase, and the re-injection phase. When the injection schedule is landed in the BC time interval, the fracture propagation speed is completely stagnant. When the injection time reaches the right side of C, the hydraulic fracture re-enters the high-speed propagation state again.

If a more efficient stimulation effect is pursued, reflected by the maximum growth of the fracture size of each cycle, the starting moment of the re-injection phase (magenta shadow area) should be chosen just after the hydraulic fracture has nearly stopped growing. This provides a new idea for optimizing the interval time of fracturing operation by cyclic injection. Considering the formation with a small fracture toughness can continuously grow in the depressurization phase and the zero-injection phase, the time interval for the re-injection cycle can be properly elongated.

Compared with the hysteretic response of hydraulic fracture propagation to the cyclic injection-rate change at a low fracture toughness K_{IC}; a high fracture toughness promotes more rapid feedback of fracture extension to the turn of

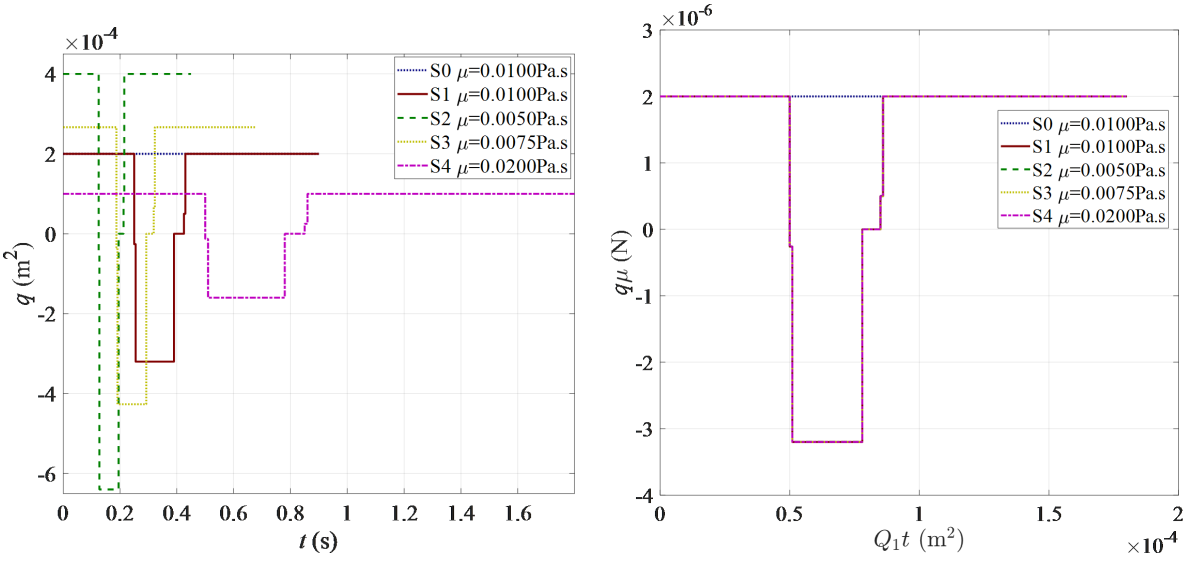

(a) (b)

Fig.12 (a) The curve of flow rate q vs time t and (b) the product of injection rate q and viscosity μ vs the product of q and T1 for different CIAF sequences S1~S4

Table 4 The parameters of numerical cases related to injection rate Q and viscosity μ

Cases	σ_1 (MPa)	σ_2 (MPa)	μ (Pa•s)	Q_1 ($m^2 \cdot s^{-1}$)	Injection type
CX1	2.8	2.0	0.010	0.0002	CIAF (schedule S1)
CX2	2.8	2.0	0.005	0.0004	CIAF (schedule S2)
CX3	2.8	2.0	0.010	0.0002	CCI (schedule S0)
CY1	4.8	2.0	0.010	0.0002	CIAF (schedule S1)
CY2	4.8	2.0	0.0075	0.000267	CIAF (schedule S3)
CY3	4.8	2.0	0.010	0.0002	CCI (schedule S0)
CZ1	6.8	2.0	0.010	0.0002	CIAF (schedule S1)
CZ2	6.8	2.0	0.020	0.0001	CIAF (schedule S4)
CZ3	6.8	2.0	0.010	0.0002	CCI (schedule S0)

Table 5 The CIAF schedule S2 (μ=0.005 Pa•s for CX2)

Time t (s)	$T_0 \le t < T_1$	$T_1 \le t < T_2$	$T_2 \le t < T_3$	$t \ge T_3$
	0 ~ 0.126	0.126 ~ 0.195	0.195 ~ 0.214	≥ 0.214
Flow rate q (m^2/s)	Q_1	Q_2	Q_3	Q_4
	4.0×10^{-4}	-6.4×10^{-4}	0	4.0×10^{-4}

Table 6 The CIAF schedule S3 (μ=0.0075 Pa•s for CY2)

Time t (s)	$T_0 \le t < T_1$	$T_1 \le t < T_2$	$T_2 \le t < T_3$	$t \ge T_3$
	0 ~ 0.189	0.189 ~ 0.293	0.293 ~ 0.321	≥ 0.321
Flow rate q (m^2/s)	Q_1	Q_2	Q_3	Q_4
	2.67×10^{-4}	-4.27×10^{-4}	0	2.67×10^{-4}

Table 7 The CIAF schedule S4 (μ=0.020 Pa•s for CZ2)

Time t (s)	$T_0 \le t < T_1$	$T_1 \le t < T_2$	$T_2 \le t < T_3$	$t \ge T_3$
	0 ~ 0.505	0.505 ~ 0.780	0.780 ~ 0.855	≥ 0.855
Flow rate q (m^2/s)	Q_1	Q_2	Q_3	Q_4
	1.0×10^{-4}	-1.6×10^{-4}	0	1.0×10^{-4}

injection rate. A faster pace of hydraulic fractures into length stagnation means that the time for a positive injection rate of each cycle can be appropriately elongated, and the depressurization and zero-injection rate phases can be further shortened, allowing for CIAF schedule to be optimized to achieve a suitable fracture length growth per injection cycle.

4.3 The product of Injection rate and fluid viscosity (q•μ)

For conventional constant-rate injection

cases, the fracturing behaviors are functions of the product of injection rate and fluid viscosity (q•μ) and the cumulative injection volume [38, 50]. However, the injection rate of the CIAF is no longer a constant value. To further explore whether the previous controlling law still works or not in CIAF, a series of numerical cases under different combinations of injection schemes and fluid viscosities are carried out, as listed in Table 4. The initial injection flow rate value Q_1 is used as a temporary representative for each CIAF schedule, and four injection schedules are used as shown in Fig.12. Particularly, the constant rate $q=Q_1=q0$ is used for conventional continuous injection (CCI) schedule S0 as reference. In those injection schedules, the flowback rates in the depressurization phase are set to be larger than the initial injection rate to allow the wellbore pressure drops to zero in a short time.

Fig.12 (a) The curve of flow rate q vs time t and (b) the product of injection rate q and viscosity μ vs the product of q and T1 for different CIAF sequences S1~S4

For the fracturing by CIAF method, the cumulative injection volume Vt at time t can be expressed as:

$$V_t = \sum_{i=1}^{n} Q_i(T_i - T_{i\text{-}1}) + Q_n(t - T_{n\text{-}1}) \qquad T_{n-1} \le t < T_n \tag{9A}$$

Where $t=T_i$ is the starting time of each corresponding injection value $q = Q_i$. When it is injected for the conventional fracturing under a constant rate (denoted q_o), the cumulative injection volume V_t at time t is

$$V_t = q_o t \tag{9B}$$

The numerical cases given in Table 4 were divided into three groups according to the in-situ stress levels. Among them, the in-situ stress σ_1 and σ_2 of the cases CX1~ CX3, CY1~CY3, CZ1~CZ3

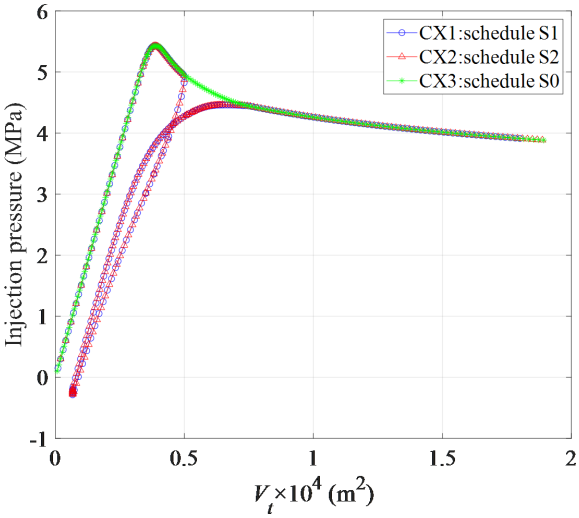

Fig.13 The injection pressure P_w vs the injection volume V_t of the cases CX1, CX2 with the CIAF schedule and CX3 with the conventional injection schedule

are 2.8 and 2.0 MPa, 4.8 and 2.0 MPa, 6.8 and 2.0 MPa, respectively. In addition, these injection schedules are deliberately chosen so that the cumulative injection volume Vt for each counterpart injection phase is the same. Meanwhile, the fluid viscosity is also consciously set to guarantee the product of Q_i•μ is the same for the corresponding phases of those injection schedules, as shown in Table 4. The CIAF schedules S1, S2, S3, S4 (See Table 5, Table 6, Table 7) after properly scaled, can eventually coincide with each other, as shown in Fig.12(b).

It can be seen from Fig.13 that although the viscosity and injection rate sequence used by CX1 and CX2 are different, the curves of injection pressure vs the cumulative injection volume Vt overlap, each other for these two cases with the same product q•μ. This coincidence occurs not only in the initial injection phase, zero injection-rate phase, and re-injection phase but also in the depressurization phase. Therefore, for cyclic injection with the same q•μ, the injection pressure P_w can be solely determined by the cumulative liquid volume Vt. Compared to the conventional

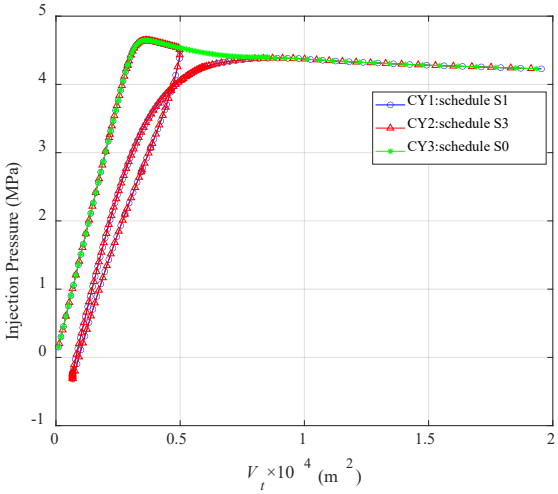

Fig.14 The injection pressure P_w vs the injection volume V_t of the cases CY1, CY2 with the CIAF schedule and CY3 with the conventional injection schedule S0

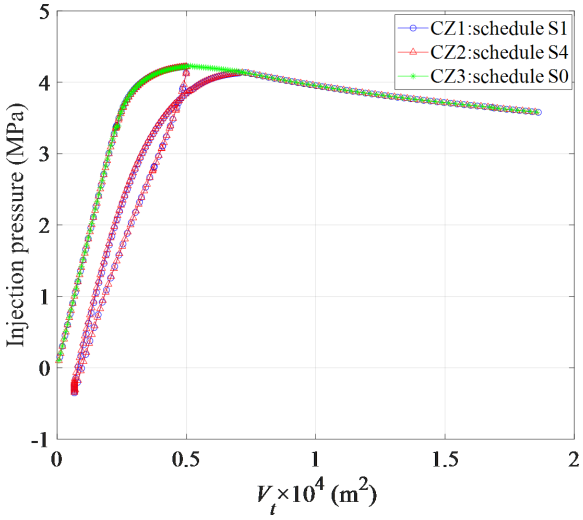

Fig.15 The injection pressure P_w vs the injection volume V_t of the cases CZ1, CZ2 with the CIAF schedule and CZ3 with the conventional injection schedule S0

constant-rate injection case CX3, the injection pressure P_w for two injection cases follows exactly the curve of CX3 at a subsequent larger time.

We have found the same features for the group of numerical cases CY1~CY3 with the far-field stresses of 4.8-2.0MPa in Fig.14, and another group containing CZ1~CZ3 with the stresses of 6.8-2.0 MPa in Fig.15.

5 Discussion

As a new approach of cyclic injection fracturing, CIAF has a much higher amplitude of cyclic pressure compared with conventional CIF by injection pressure or injection rate. Normally, cyclic injection under injection-pressure controlled mode, with very limited cyclic pressure amplitude, taking granite rock for instance, typically requires 50 to 150 cycles to initiate wellbore and create multiple fractures [6]. While the fracturing experiments using the CIAF method produce complex hydraulic fractures under no more than 13 cycles according to our previous studies [7, 51]. This highlights the strength of CIAF in the field application.

In the actual CIAF operation for hydrocarbon reservoirs, the flowback fluid in every injection cycle can be collected and recycled to frack the formation in the next injection cycle. The recycled fluid would save the demand for additional fracturing fluid. Fig.16 illustrates the concept of this new strategy. In a conventional fracturing operation, the fracturing fluid is pumped from the fluid tank, mixed with the proppant by the blender trucks, which is pressurized by the fracturing truck and injected into the ground through a high-pressure manifold. After the fracturing is completed, the fracturing fluid is depressurized and poured into the flowback pool. On the basis of the conventional fracturing injection operation, we recollect the flowback fracturing fluid through a pump, and mix it with the original fracturing fluid through the pipeline, then re-inject it into the ground. Then repeat the above operation and so forth until almost all the fracturing fluid and flowback fluid can be injected into the target reservoir in-depth.

Based on the above analysis we performed,

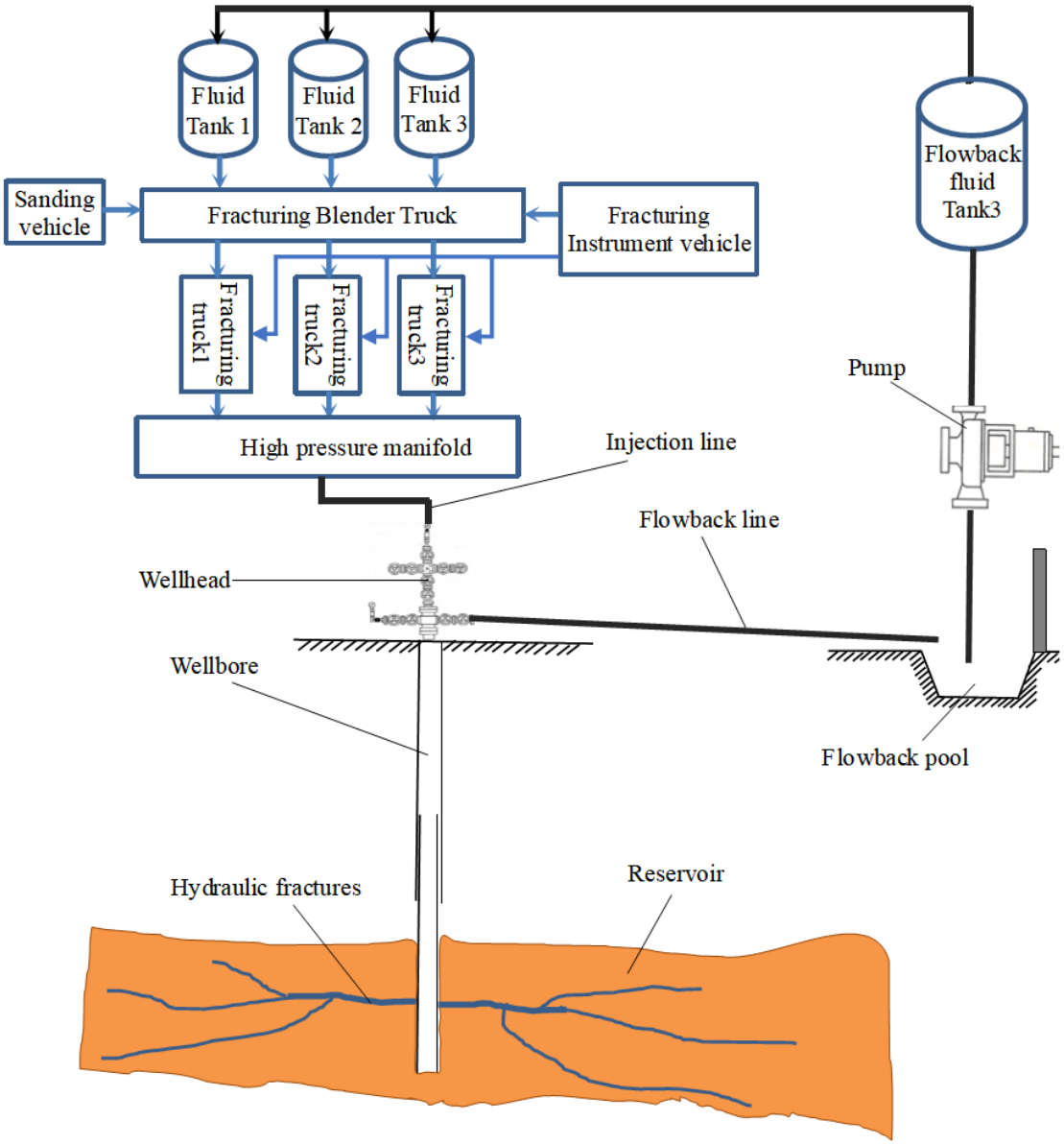

Fig.16 The field operation sketch of the fracturing method by CIAF

even in the depressurization phase with a flowback operation, the fracture still grows meanwhile a significant part of flowback fluid can be collected and reused for fracturing in the following injection cycles. Thus, more water can probably be saved. It is known that hydraulic fracturing for unconventional oil/gas reservoirs consumes a huge amount of water, which arouses many environmental concerns [52, 53]. How to reduce the need for water and maximize the efficiency of the fracturing fluid is still an important issue we need to address. Based on the suitable growth of the fracture length in each cycle, the time interval of the cyclic injection can be optimized.

The advantage of this operation method can achieve a relative balance between the operational

efficiency and effect of fracture creation. Moreover, all the flowback fluid can be reused to generate new fractures, and finally, almost zero-wastewater discharge (not flow-back fluid for the last cycle) can be fulfilled. The process is economic sustainability and environmentally friendly.

The fracture behavior patterns under CIAF distinguishing from the conventional continuous injection provided us with a new view associated with the cyclic injection. Note that in the CIAF, a fast flowback operation renders a higher internal fracture pressure. This feature is expected to be beneficial for the generation of multi-fracture in real formation, given the formation involves natural fractures and weak layers such as in shale formations. Cyclic injection fracturing involves the rock strength deterioration subject to the cyclic hydraulic pressure and cleavage of subcritical cracks. Considering its prohibitive complexity, this paper does not include this part of the study.

6 Conclusions

In this paper, a cyclic fracturing method using the CIAF method with high fracture-creating efficiency and environmental sustainability is proposed. It is implemented by collecting the flowback fluid for secondary utilization and re-injecting it into formation to create new fractures in the subsequent cycles. In our numerical study, using the displacement discontinuity method (DDM), the analysis of hydraulic fracture growth of different phases of CIAF and related parametric studies including fracture internal pressure, fracture width, and injection pressure is performed. The conclusions are as follows:

(1) In the depressurization phase by flowback, the fracture still continues to extend, and the fracture mouth closes faster as the wellbore pressure drops to the lowest point. In the zero injection-rate phase, due to the closure of the fracture mouth, a part of the liquid is sealed inside the fracture with the internal pressure rising under the confined compression of the surrounding rock matrix. The fast flowback provides an impetus for the rising of the internal pressure of the fracture accompanied by the fracture's continuous growth. As to the re-injection phase, there is a trough of the internal pressure of the fracture. The location of the trough pressure moves from the wellbore to the fracture tip until the fracture growth resumes. Even deep inside the fracture, the pressure loading on the fracture surface is in a cyclic variation state with a comparable amplitude in contrast with the injection pressure amplitude.

(2) When subject to different in situ stresses, a smaller stress difference with the same minimum stress is accompanied by a narrower fracture mouth width. Except for the slight difference in the primary fracture initiation moment, the fracture extension over time tends to be insensitive to the in-situ stress. The fracture mouth width is insensitive to the fracture toughness. The higher fracture toughness often renders a slightly higher injection pressure. Smaller fracture toughness can promote the faster growth speed of the fracture, but get more difficult to be stunted fracture extension even in the depressurization and zero injection rate phases.

(3) The curves of the injection pressure P_w vs the cumulative injection volume Vt coincide with each other through the whole cycle injection process under the same corresponding product of the flow rate and the fluid viscosity $Q_i \bullet \mu$. The injection pressure curve P_w vs Vt after cyclic injection segment also follows exactly the curve of constant-rate injection case at subsequent large time. The cumulative injection volume Vt thus becomes an important factor to characterize fracturing behavior under cyclic injection, instead

of the injection time.

In this numerical model, solid rock is regarded as a homogeneous material. based on the numerical results, it is expected that natural fissures in the rock may be activated to the maximum degree under cyclic injection, and then initiated to form complex fractures. This is because that rock is a natural material with many micro-cracks and defects. This will be our future work for the next step.

Acknowledgement

The author sincerely thanks all the financial support.

Funding Statement

China Academy of Engineering Regional Cooperation Project: “Strategic Research on the Leapfrog Development of Guangxi Shale Gas Industry” (Grant No. GXYD24310009)

Xinjiang Uygur Autonomous Region “Tianshan Talents” Training Program—Science and Technology Innovation Team Project (Grant No. 2024TSYCTD0018)

Guangxi Key Research and Development Program: “Geological Theory and Engineering Technology Research of the First Shale Gas Demonstration Project in Guangxi” (Grant No. AB24010088)

National Natural Science Foundation of China (Grant NO.52204055).

Author Contributions

The authors confirm their responsibility for the following: study conception and design, data collection, analysis and interpretation of results, and manuscript preparation.

Availability of Data and Materials

None.

Conflicts of Interest

The authors declare that they have no conflicts of interest to report regarding the present study.

References

[1] Warpinski, N.R. and Teufel, L.W., Influence of Geologic Discontinuities on Hydraulic Fracture Propagation. Journal of Petroleum Technology, 1987. 39(2): 209-220.

[2] Olasolo, P., Juárez, M., Morales, M., et al., Enhanced geothermal systems (EGS): A review. Renewable and Sustainable Energy Reviews, 2016. 56: 133-144.

[3] Sinclair, L. and Thompson, J., In situ leaching of copper: Challenges and future prospects. Hydrometallurgy, 2015. 157: 306-324.

[4] Bunger, A. and Lecampion, B., Four critical issues for successful hydraulic fracturing applications. Rock mechanics and engineering, 2017(BOOK_CHAP).

[5] Lee, K.-K., Ellsworth, W.L., Giardini, D., et al., Managing injection-induced seismic risks. Science, 2019. 364(6442): 730-732.

[6] Zhuang, L., Kim, K.Y., Jung, S., et al. Laboratory study on cyclic hydraulic fracturing of Pocheon granite in Korea. in the 50th US Rock Mechanics / Geomechanics Symposium. 2016.

[7] Zhou, Z.L., Zhang, G.Q., Dong, H.R., et al., Creating a network of hydraulic fractures by cyclic pumping. International Journal of Rock Mechanics and Mining Sciences, 2017. 97(9): 52-63.

[8] Hulse, D.S., Fracturing process with superimposed cyclic pressure. 1959, U.S. Patent

[9] Zhuang, L., Jung, S.G., Diaz, M., et al., Laboratory True Triaxial Hydraulic Fracturing of Granite Un-

der Six Fluid Injection Schemes and Grain-Scale Fracture Observations. Rock Mechanics and Rock Engineering, 2020. 53(10): 4329-4344.

[10] Chen, J., Cao, H., Sun, P., et al., Mechanisms of fracture extending in coal rock by pulse hydraulic fracturing under triaxial loading. Rock and Soil Mechanics, 2017. 38(4): 1023-1031.

[11] Wei, C., Zhang, B., Li, S.C., et al., Interaction between Hydraulic Fracture and Pre-Existing Fracture under Pulse Hydraulic Fracturing. Spe Production & Operations, 2021. 36(3): 553-571.

[12] Wu, F., Pu, C., Chen, D., et al., Coupling simulation of multistage pulse conflagration compression fracturing. Petroleum Exploration and Development, 2014. 41(5): 663-670.

[13] Yoon, J.S., Zang, A., and Stephansson, O., Numerical investigation on optimized stimulation of intact and naturally fractured deep geothermal reservoirs using hydro-mechanical coupled discrete particles joints model. Geothermics, 2014. 52(10): 165-184.

[14] Yoon, J.S., Zimmermann, G., and Zang, A., Discrete element modeling of cyclic rate fluid injection at multiple locations in naturally fractured reservoirs. International Journal of Rock Mechanics and Mining Sciences, 2015. 74(5): 15-23.

[15] Zang, A., Stephansson, O., Stenberg, L., et al., Hydraulic fracture monitoring in hard rock at 410 m depth with an advanced fluid-injection protocol and extensive sensor array. Geophysical Journal International, 2016. 208(2): 790-813.

[16] Zang, A., Yoon, J.S., Stephansson, O., et al., Fatigue hydraulic fracturing by cyclic reservoir treatment enhances permeability and reduces induced seismicity. Geophysical Journal International, 2013. 195(2): 1282-1287.

[17] Zhuang, L., Kim, K.Y., Jung, S.G., et al., Cyclic hydraulic fracturing of pocheon granite cores and its impact on breakdown pressure, acoustic emission amplitudes and injectivity. International Journal of Rock Mechanics and Mining Sciences, 2019. 122(10): 104065.

[18] Diaz, M., Jung, S.G., Zhuang, L., et al. Comparison of Acoustic Emission Activity in Conventional and Cyclic Hydraulic Fracturing in Cubic Granite Samples Under Tri-Axial Stress State. in 52nd U.S. Rock Mechanics/Geomechanics Symposium. 2018.

[19] Patel, S.M., Sondergeld, C.H., and Rai, C.S., Laboratory studies of hydraulic fracturing by cyclic injection. International Journal of Rock Mechanics and Mining Sciences, 2017. 95(5): 8-15.

[20] Zimmermann, G., Moeck, I., and Blöcher, G., Cyclic waterfrac stimulation to develop an Enhanced Geothermal System (EGS)—Conceptual design and experimental results. Geothermics, 2010. 39(1): 59-69.

[21] Suresh, S., Fatigue of materials. 1998: Cambridge university press.

[22] Singh, S.K., Fatigue and strain hardening behaviour of graywacke from the flagstaff formation, New South Wales. Engineering Geology, 1989. 26(2): 171-179.

[23] Ghamgosar, M. and Erarslan, N., Experimental and Numerical Studies on Development of Fracture Process Zone (FPZ) in Rocks under Cyclic and Static Loadings. Rock Mechanics and Rock Engineering, 2016. 49(3): 893-908.

[24] Haimson, B. and Fairhurst, C. In-situ stress determination at great depth by means of hydraulic fracturing. in The 11th US symposium on rock mechanics (USRMS). 1969. OnePetro.

[25] Stock, J., Healy, J., Hickman, S., et al., Hydraulic fracturing stress measurements at Yucca Mountain, Nevada, and relationship to the regional stress field. Journal of Geophysical Research: Solid Earth, 1985. 90(B10): 8691-8706.

[26] Zoback, M., Barton, C., Brudy, M., et al., Determination of stress orientation and magnitude in deep wells. International Journal of Rock Mechanics and Mining Sciences, 2003. 40(7-8): 1049-1076.

[27] Hickman, S. and Zoback, M., Stress measurements in the SAFOD pilot hole: implications for the frictional strength of the San Andreas fault. Geophys. Res. Lett, 2004. 31: L15S12.

[28] Crouch, S.L., Starfield, A.M., and Rizzo, F.J., Boundary Element Methods in Solid Mechanics. Journal of Applied Mechanics, 1983. 50(3): 704.

[29] Zhang, X. and Jeffrey, R.G., Numerical studies on crack problems in three-layered elastic media using an image method. International Journal of Fracture, 2006. 139(3-4): 477-493.

[30] Zhang, X., Jeffrey, R.G., and Thiercelin, M., Deflection and propagation of fluid-driven fractures at frictional bedding interfaces: A numerical investigation. Journal of Structural Geology, 2007. 29(3): 396-410.

[31] Zhang, X., Jeffrey, R.G., and Detournay, E., Propagation of a hydraulic fracture parallel to a free surface. International Journal for Numerical and Analytical Methods in Geomechanics, 2005. 29(13): 1317-1340.

[32] Zhang, X., Jeffrey, R.G., and Thiercelin, M., Mechanics of fluid-driven fracture growth in naturally fractured reservoirs with simple network geometries. Journal of Geophysical Research: Solid Earth, 2009. 114(B12).

[33] Hills, D., Kelly, P., Dai, D.N., et al., Solution of Crack Problems. The Distributed Dislocation Technique. Vol. 44. 1996.

[34] Olson J., E., Fracture aperture, length and pattern geometry development under biaxial loading: a numerical study with applications to natural, cross-jointed systems. Geological Society London Special Publications, 2007. 289(1): 123-142.

[35] Erdogan, F. and Sih, G.C., On the Crack Extension in Plates Under Plane Loading and Transverse Shear. Journal of Basic Engineering, 1963. 85(4): 519.

[36] Kear, J., Kasperczyk, D., Zhang, X., et al. 2D Experimental and Numerical Results for Hydraulic Fractures Interacting With Orthogonal and Inclined Discontinuities. in 51st U.S. Rock Mechanics/Geomechanics Symposium. 2017.

[37] Cheng, S., Zhang, M., Zhang, X., et al., Numerical study of hydraulic fracturing near a wellbore using dual boundary element method. International Journal of Solids and Structures, 2022. 239-240: 111479.

[38] Zhang, X., Jeffrey, R.G., Bunger, A.P., et al., Initiation and growth of a hydraulic fracture from a circular wellbore. International Journal of Rock Mechanics and Mining Sciences, 2011. 48(6): 984-995.

[39] Lecampion, B., Peirce, A., Detournay, E., et al. The Impact of the Near-Tip Logic on the Accuracy and Convergence Rate of Hydraulic Fracture Simulators Compared to Reference Solutions. in ISRM International Conference for Effective and Sustainable Hydraulic Fracturing. 2013.

[40] Detournay, E., Propagation Regimes of Fluid-Driven Fractures in Impermeable Rocks. International Journal of Geomechanics, 2004. 4(1): 35-45.

[41] Jeffrey, R.G., Kear, J., Kasperczyk, D., et al. A 2D Experimental Method with Results for Hydraulic Fractures Crossing Discontinuities. in 49th U.S. Rock Mechanics/Geomechanics Symposium. 2015.

[42] Zhang, L., Wu, B., Zhang, X., et al., An Analytical Model for Predicting Temperature Fields during Fluid Circulation in a Deep-Sea Well. SPE Journal, 2022. 27(01): 167-185.

[43] Ranjith, P.G., Wanniarachchi, W.A.M., Perera, M.S.A., et al., Investigation of the effect of foam flow rate on foam-based hydraulic fracturing of shale reservoir rocks with natural fractures: An experimental study. Journal of Petroleum Science and Engineering, 2018. 169: 518-531.

[44] Jung, Y., Doughty, C., Borgia, A., et al., Pressure transient analysis during CO2 push-pull tests into faults for EGS characterization. Geothermics, 2018. 75: 180-191.

[45] Atkinson, B.K., Subcritical crack growth in geological materials. Journal of Geophysical Research: Solid Earth, 1984. 89(B6): 4077-4114.

[46] Atkinson, B.K. and Meredith, P.G., The Theory of Subcritical Crack Growth with Applications to Minerals and Rocks, in Fracture Mechanics of Rock, B.K. Atkinson, Editor. 1987, Academic Press: London. 111-166.

[47] Bunger, A.P. and Lu, G., Time-Dependent Initiation of Multiple Hydraulic Fractures in a Formation With Varying Stresses and Strength. SPE Journal, 2015. 20(06): 1317-1325.

[48] Olson, J.E., Joint pattern development: Effects of subcritical crack growth and mechanical crack interaction. Journal of Geophysical Research: Solid Earth, 1993. 98(B7): 12251-12265.

[49] Kong, L., Ranjith, P.G., and Li, B.Q., Fluid-driven micro-cracking behaviour of crystalline rock using a coupled hydro-grain-based discrete element method. International Journal of Rock Mechanics and Mining Sciences, 2021. 144: 104766.

[50] Lecampion, B., Desroches, J., Jeffrey, R.G., et al., Experiments versus theory for the initiation and propagation of radial hydraulic fractures in low-permeability materials. Journal of Geophysical Research-Solid Earth, 2017. 122(2): 1239-1263.

[51] Zhou, Z.L., Zhang, G.Q., Xing, Y.K., et al., A Laboratory Study of Multiple Fracture Initiation from Perforation Clusters by Cyclic Pumping. Rock Mechanics and Rock Engineering, 2019. 52(3): 827-840.

[52] Chen, H. and Carter, K.E., Water usage for natural gas production through hydraulic fracturing in the United States from 2008 to 2014. Journal of Environmental Management, 2016. 170: 152-159.

[53] Zhang, D. and Yang, T., Environmental impacts of hydraulic fracturing in shale gas development in the United States. Petroleum Exploration and Development, 2015. 42(6): 801-807.